Research in Astronomy and Astrophysics, 25:025002 (10pp), 2025 February

https://doi.org/10.1088/1674-4527/ad7a58
CSTR: 32081.14.RAA.ad7a58

GRB 201223A: Implication of Fallback Accretion onto the Newborn Black Hole from its Multiband Afterglow

Tian-Hua Lu[1,2], Dong Xu[1], Wei-Hua Lei[3], Shao-Yu Fu[1,2], Shuai-Qing Jiang[1,2], Zi-Pei Zhu[1], Xing Liu[1,2], and Jie An[1,2]
[1] Key Laboratory of Space Astronomy and Technology, National Astronomical Observatories, Chinese Academy of Sciences, Beijing 100101, China; dxu@nao.cas.cn
[2] School of Astronomy and Space Science, University of Chinese Academy of Sciences, Chinese Academy of Sciences, Beijing 100049, China
[3] Department of Astronomy, School of Physics, Huazhong University of Science and Technology, Wuhan 430074, China
Received 2024 March 25; revised 2024 April 24; accepted 2024 April 29; published 2025 January 22

Abstract

Multiband afterglow observations of gamma-ray bursts (GRBs) are important for studying the central engine. GRB 201223A is a GRB with prompt optical detection by GWAC. Here we report on the early optical afterglow of GRB 201223A detected by NEXT (only 2.8 minutes after the Swift/BAT trigger), which smoothly connects the prompt optical emission and the afterglow phase. Utilizing Amati diagrams and considering the detection of afterglow emission in the Swift *u*-band, we suggest a redshift range of 0.26–1.85. Based on our optical data and combined with early optical observation from GWAC and early X-ray data from Swift/XRT, a multiband fitting is performed using `PyFRS`, and we obtain the best afterglow parameters (assuming a redshift of $z = 1.0$): $E_{\rm K,iso} = 5.01^{+1.91}_{-1.70} \times 10^{54}$ erg, $\Gamma_0 = 426.58^{+148.86}_{-138.18}$, $\theta_{\rm j} = 25.98^{+9.67}_{-10.54}$ deg, $n_0 = 0.30^{+3.78}_{-0.26}$ cm^{-3}, $p = 2.32^{+0.01}_{-0.01}$, $\epsilon_{\rm e} = 3.31^{+1.59}_{-0.86} \times 10^{-5}$, $\epsilon_{\rm B} = 3.47^{+4.12}_{-2.62} \times 10^{-1}$. The late-time X-ray shows a re-brightening, indicating late-time central engine activities. After comparing the leading two central engine models, i.e., magnetar model and hyperaccreting black hole model, we find that the fallback accretion onto a newborn black hole provides a better explanation for the X-ray re-brightening with fallback accretion rate $\dot{M}_{\rm p} \simeq 2.76 \times 10^{-9} M_{\odot}$ s^{-1} and the total fallback accreted mass $M_{\rm fb} \simeq 1.41 \times 10^{-6} M_{\odot}$.

Key words: GRB: central engine – GRB: afterglow – GRB: GRB 201223A

1. Introduction

A gamma-ray burst (GRB) is a phenomenon in which the gamma-ray intensity dramatically increases and decreases in space. Based on the statistics of prompt emission duration timescale (T_{90}) and the spectral hardness of the bursts, GRBs can be classified into two groups: long bursts with $T_{90} > 2$ s and short bursts with $T_{90} < 2$ s (Kouveliotou et al. 1993; Paciesas et al. 1999). It is generally accepted that long bursts arise from the collapse of massive stars and are associated with broad-lined Type Ic supernovae (Galama et al. 1999; Woosley & Bloom 2006), while short bursts arise from the merger of neutron stars (NSs) associated with kilonovae (Kouveliotou et al. 1993; Zhang et al. 2009; Abbott et al. 2017). However, the central engine of GRBs remains an open question.

X-rays and optical afterglow of GRB were discovered in 1997. The first discovery of the optical afterglow of a GRB came after BeppoSAX detected the X-ray afterglow of GRB 970228, the optical afterglow of which was detected by ground-based telescopes on March 8 of that year (Costa et al. 1997). BeppoSAX detected a total of 1082 GRBs between 1996 and 2003 (Zhang 2018). Although many GRBs have been discovered, only a very small number of them have optical follow-up observations. The main reason is the long interval between the discovery of a GRB and the corresponding ground-based optical follow-up, which misses the early bright phase. The Neil Gehrels Swift Observatory (Swift hereafter) was successfully launched in 2004 (Gehrels et al. 2004). Swift carries three instruments: the Burst Alert Telescope (BAT), the X-Ray Telescope (XRT), and the Ultraviolet/Optical Telescope (UVOT). Swift transmits the location of a detected GRB to ground stations within approximately 10 s. Subsequently, the XRT and UVOT instruments autonomously slew (reposition) toward the GRB direction within about 100 s. This rapid response sequence significantly enhances the capability for multi-wavelength follow-up observations of GRBs. The rich multiband afterglow (from radio to X-ray, lasting up to years) data could provide us with insight into the GRB central engines.

The afterglow phase is later than the prompt emission phase. The lack of prompt optical emissions of GRBs has severely limited our understanding of the transition between the two phases. The transition of prompt-to-afterglow emission in the optical band was first observed in GRB 050820A, which lasted for over 750 s (Vestrand et al. 2006). Recently, Xin et al. (2023) reported the detection of prompt optical emissions from GRB 201223A using Ground-based Wide Angle Camera

(GWAC). This successful detection supports the idea that large field-of-view (FOV) instruments can capture bright but short-duration signals from GRBs. They argued that the transition between prompt emission and afterglow in optical of GRB 201223A is smooth and there is no sign of late central engine activities.

However, the late X-ray afterglow of GRB 201223A is contaminated by a flaring or plateau-like re-brightening behavior, which should be linked to the central engine activities. A systematic analysis of the Swift GRB X-ray afterglow showed that bursts with X-ray plateau followed by a steep decay ($\alpha \geqslant 3$) are most likely driven by rapidly spinning magnetars (Liang et al. 2007; Tang et al. 2019; Zhao et al. 2019). For those with giant bumps, the central engine with fallback accretion onto a newborn black hole (BH) is preferred (Wu et al. 2013; Gao et al. 2016a; Zhao et al. 2021; Zhao 2023). Such a hyperaccreting BH system can launch a relativistic jet via the Blandford–Znajek (BZ) mechanism (Blandford & Znajek 1977; Lei et al. 2005a; Liu et al. 2015, 2017). Some GRB X-ray afterglows show two plateaus (Chen et al. 2017; Zhao et al. 2020) which provide support to the magnetar central engine model. Therefore, the nature of the central engine for GRB 201223A, i.e., a millisecond magnetar or a fallback accretion BH, deserves detailed study.

In this work, we present our optical photometric observations of GRB 201223A with the Ningbo Bureau of Education and Xinjiang Observatory Telescope (NEXT) and Nordic Optical Telescope (NOT), which provide a smooth connection between the prompt optical data and the afterglow. We then investigate the central engine of GRB 201223A by combining our data with the Swift/XRT and Swift/BAT data, and other observations from GRB Coordinates Network (GCN) reports. The layout of this paper is as follows: We describe our multiband observations in Section 2. The combined analysis of multiband data is presented in Section 3. We first consider the redshift range of the burst and compare two central engine models in Section 4. A standard cosmology model is adopted with $H_0 = 67.3\,\mathrm{km\,s^{-1}\,Mpc^{-1}}$, $\Omega_M = 0.315$, $\Omega_\Lambda = 0.685$ (Planck Collaboration et al. 2014).

2. Observations

GRB 201223A first triggered Swift/BAT (Barthelmy et al. 2005) at 17:58:26 UT on 2020 December 23th, and it also triggered the high-energy satellite Fermi/Gamma-ray Burst Monitor (GBM, Wood & Team et al. 2020). The spectrum is adequately fitted by a Band function (Band et al. 1993) with a peak energy of $E_{\rm peak} = 86 \pm 12$ keV, a fixed low-energy index of $\alpha = 0.14 \pm 0.38$, and a high-energy index of $\beta = -2.6 \pm 0.4$. This model yields a 10–1000 keV fluence of $(2.1 \pm 0.3) \times 10^{-6}\,\mathrm{erg\,cm^{-2}}$. Swift/XRT began observation 73.7 s after the BAT trigger and found a bright, uncataloged X-ray source within the BAT error circle. UVOT (Roming et al. 2005) found a source with a white band magnitude 16.16 at coordinate: R.A., decl. (J2000) = $08^{\rm h}51^{\rm m}09\overset{\rm s}{.}51$, $+71°10'47\overset{''}{.}4$. The burst location in the first NEXT image is shown in Figure 1. In order to examine the full light curve of GRB 201223A, we downloaded the 0.3–10 keV data from the UK Swift Science Data Centre.[4] We also collected GWAC data from Xin et al. (2023). The multiband light curve of GRB 201223A is displayed in Figure 2.

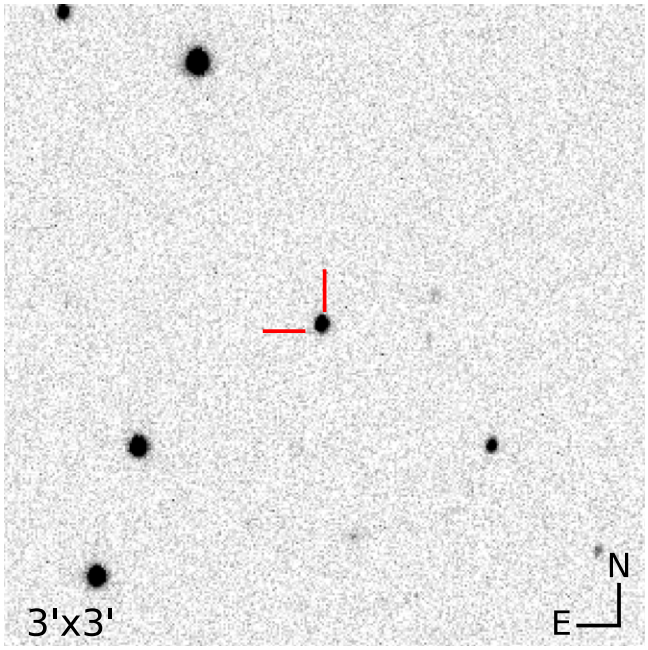

Figure 1. The r-band position of GRB 201223A within the $3' \times 3'$ FOV.

We checked the Legacy Survey (Dey et al. 2019), Sloan Digital Sky Survey (SDSS, Almeida et al. 2023) and the Wide-field Infrared Survey Explorer (WISE, Wright et al. 2010), specifically focusing on the XRT error circle. Regrettably, our investigation yielded no evidence of any sources within this designated area.

2.1. Fermi/GBM and Swift/BAT Data Reduction

The Swift/BAT data were downloaded from the UK Swift Science Data Centre. The `batbinevt` was used to generate light curve file and pha file for spectral analysis. The Fermi/GBM payload carries 12 sodium iodide (NaI, 8 keV–1 MeV) and two bismuth germanate (BGO, 200 keV–40 MeV) scintillation detectors (Meegan et al. 2009). Considering the detectors' direction of pointing, we employed two NaI detectors (n7, n8) and one BGO detector (b1) to conduct the spectral analysis. We obtained the Time-Tagged Event (TTE)

[4] https://www.swift.ac.uk/swift_portal/

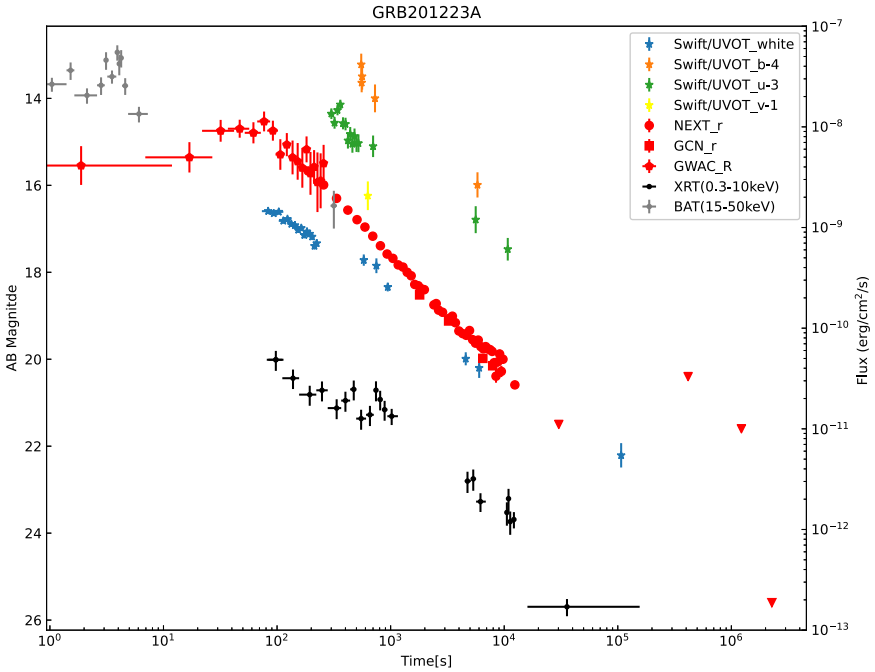

Figure 2. The multiband light curve of GRB 201223A.

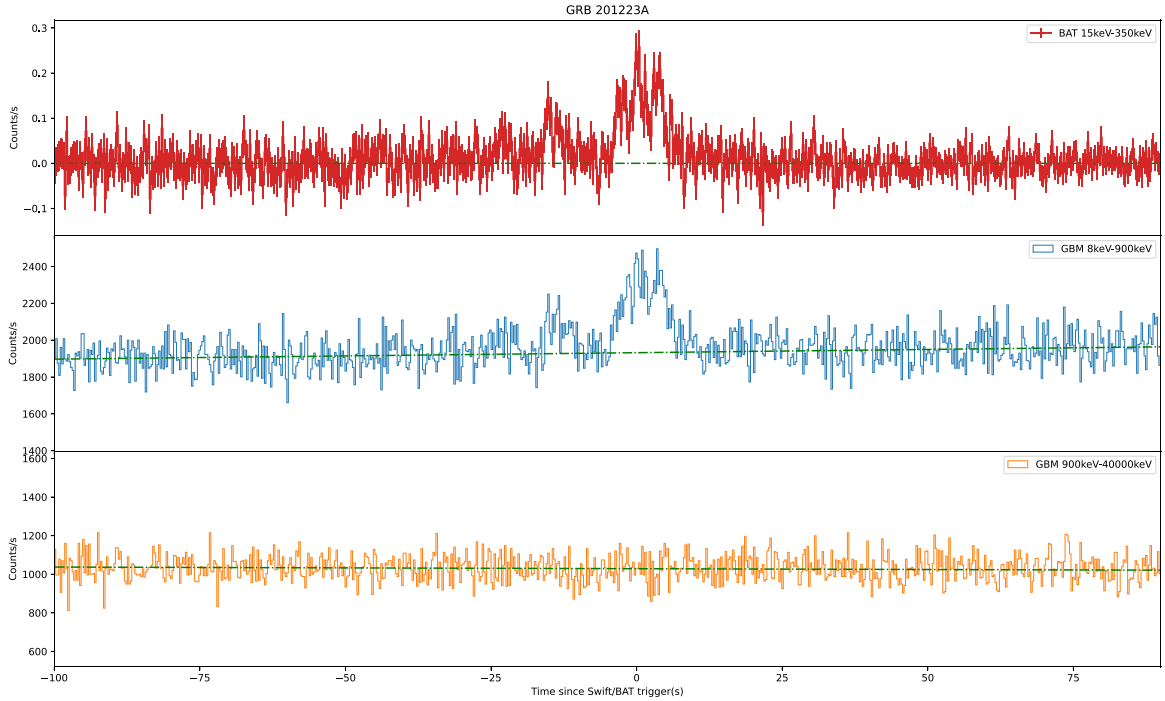

Figure 3. The prompt emission light curves of GRB 201223A in different energy channels were obtained using Swift/BAT and Fermi/GBM observations.

Table 1
The Photometric Results of NEXT and NOT

$T_{\rm mid}$ (s)	Exp (s)	Filter	Mag (AB)	Telescope	$T_{\rm mid}$ (s)	Exp (s)	Filter	Mag (AB)	Telescope
188	40	*r*	15.67 ± 0.01	NEXT	5268	300	*r*	19.55 ± 0.07	NEXT
257	40	*r*	15.99 ± 0.01	NEXT	5587	300	*r*	19.6 ± 0.08	NEXT
334	60	*r*	16.30 ± 0.01	NEXT	5906	300	*r*	19.56 ± 0.07	NEXT
420	60	*r*	16.57 ± 0.02	NEXT	6224	300	*r*	19.71 ± 0.08	NEXT
506	60	*r*	16.79 ± 0.02	NEXT	6544	300	*r*	19.76 ± 0.08	NEXT
594	60	*r*	16.96 ± 0.02	NEXT	6865	300	*r*	19.71 ± 0.08	NEXT
696	90	*r*	17.17 ± 0.02	NEXT	7190	300	*r*	19.76 ± 0.08	NEXT
813	90	*r*	17.39 ± 0.02	NEXT	7510	300	*r*	19.78 ± 0.08	NEXT
931	90	*r*	17.58 ± 0.02	NEXT	7830	300	*r*	19.82 ± 0.09	NEXT
1047	90	*r*	17.68 ± 0.03	NEXT	8150	300	*r*	20.08 ± 0.11	NEXT
1166	90	*r*	17.83 ± 0.03	NEXT	8470	300	*r*	20.39 ± 0.15	NEXT
1284	90	*r*	17.88 ± 0.03	NEXT	8790	300	*r*	20.06 ± 0.11	NEXT
1399	90	*r*	18.00 ± 0.04	NEXT	9111	300	*r*	19.88 ± 0.10	NEXT
1516	90	*r*	18.08 ± 0.04	NEXT	9431	300	*r*	20.28 ± 0.13	NEXT
1630	90	*r*	18.28 ± 0.05	NEXT	9751	300	*r*	20.00 ± 0.10	NEXT
1750	90	*r*	18.31 ± 0.05	NEXT	10811	300	*r*	20.56 ± 0.16	NEXT
2643	90	*r*	18.87 ± 0.05	NEXT	11133	300	*r*	20.33 ± 0.13	NEXT
2864	90	*r*	18.92 ± 0.06	NEXT	11452	300	*r*	20.50 ± 0.15	NEXT
1868	90	*r*	18.38 ± 0.05	NEXT	11774	300	*r*	20.25 ± 0.12	NEXT
2405	90	*r*	18.75 ± 0.08	NEXT	12094	300	*r*	20.30 ± 0.12	NEXT
1981	90	*r*	18.40 ± 0.06	NEXT	12414	300	*r*	20.53 ± 0.15	NEXT
2518	90	*r*	18.72 ± 0.07	NEXT	12733	300	*r*	20.69 ± 0.18	NEXT
3274	200	*r*	19.06 ± 0.07	NEXT	13052	300	*r*	20.72 ± 0.18	NEXT
3496	200	*r*	19.01 ± 0.06	NEXT	13371	300	*r*	20.79 ± 0.19	NEXT
3717	200	*r*	19.16 ± 0.07	NEXT	13691	300	*r*	20.98 ± 0.23	NEXT
3990	300	*r*	19.35 ± 0.07	NEXT	14009	300	*r*	20.74 ± 0.19	NEXT
4311	300	*r*	19.41 ± 0.07	NEXT	12410	300	*r*	20.59 ± 0.07	NEXT
4631	300	*r*	19.45 ± 0.07	NEXT	30340.2	120	*r*	>22.0	NOT
4949	300	*r*	19.34 ± 0.07	NEXT	2273272.46	360	*r*	>25.6	NOT

Note. $T_{\rm mid}$ (s) is the middle time of the exposure after the BAT trigger. Exp is the exposure time. All data are calibrated using nearby PS1 reference stars and not corrected for Galactic extinction, which is $E(B-V) = 0.04$ mag.

data covering the time range of this GRB from the Fermi/GBM public data archive.[5]

The 256 ms time-bin light curves in different energy bands are shown in Figure 3. A joint analysis was performed via *threeML* (Vianello et al. 2015) for the Swift/BAT data and Fermi/GBM data with Band function model (Band et al. 1993)

$$N(E) = \begin{cases} A\left(\frac{E}{100\ \rm keV}\right)^{\alpha} \exp\left(-\frac{E}{E_0}\right), & E < (\alpha-\beta)E_0 \\ A\left(\frac{(\alpha-\beta)E_0}{100\ \rm keV}\right)^{\alpha-\beta} \exp(\beta-\alpha)\left(\frac{E}{100\ \rm keV}\right)^{\beta}, & E \geqslant (\alpha-\beta)E_0, \end{cases}$$

where A is the normalization of the spectrum, E_0 is the break energy in the spectrum, and α and β are the low-energy and high-energy photon spectral indices, respectively.

2.2. NEXT Optical Observations

NEXT is an equatorial telescope located at Nanshan, Xinjiang, China. NEXT began its observation on 2017 November. The telescope has a 60 cm aperture and the FOV is $22' \times 22'$. The size of the CCD is 2048×2048 pixels with a pixel size of 15 μm. The pixel scale is $0\farcs64$ pixel^{-1} (Zhu et al. 2023a). The typical gain is $1.85e^-$/ADU and the usual readout noise is $13e^-$ with 500 kHz readout speed. With images having 30 minute exposures, the typical limiting magnitude can reach 21.5. NEXT is equipped with *BV* filters in the standard Johnson-Cousins system and *griz* filters and a white filter in the Sloan system.

NEXT began to obtain the first image of GRB 201223A at 18:01:14 UT, 2.8 minutes after the BAT trigger (Zhu et al. 2020). We obtained 57 images on 2020 December 23rd, all in the *r* filter. The exposure times were 2×40 s, 4×60 s, 16×90 s, 3×200 s, and 30×300 s. The observing mid-time and exposure time of each frame are presented in Table 1.

2.3. NOT Optical Observations

NOT has an aperture of 2.56 m, and is located in La Palma, Canary Islands, Spain. Routine observations started in 1990 with Alhambra Faint Object Spectrograph and Camera

[5] https://heasarc.gsfc.nasa.gov/FTP/fermi/data/gbm/daily/

Table 2
The Input Parameters, Prior Type, Prior Range, and Best-fit Value of Multiband Modeling of GRB 201223A were Generated with `PyFRS`

Parameter	Prior Type	Prior Range	**Best Fit**
$E_{\rm K,iso}$ (erg)	log-uniform	$[10^{51}, 10^{56}]$	$5.01^{+1.91}_{-1.70} \times 10^{54}$
Γ_0	log-uniform	[10, 2000]	$426.58^{+148.86}_{-138.18}$
$\theta_{\rm j}$ (deg)	uniform	[0.01, 40]	$25.98^{+9.67}_{-10.54}$
n_0 ($\rm cm^{-3}$)	log-uniform	$[10^{-4}, 10^{3}]$	$0.30^{+3.78}_{-0.26}$
p	uniform	[2.01, 3]	$2.32^{+0.01}_{-0.01}$
$\epsilon_{\rm e}$	log-uniform	$[10^{-6}, 1]$	$3.31^{+1.59}_{-0.86} \times 10^{-5}$
$\epsilon_{\rm B}$	log-uniform	$[10^{-6}, 1]$	$3.47^{+4.12}_{-2.62} \times 10^{-1}$

(ALFOSC) and NOTCam. The ALFOSC imager can be used for imaging observations, taking low and medium resolution and polarization observations. ALFOSC has an FOV of $6\farcm4 \times 6\farcm4$ in imaging mode and is equipped with a Johnson-Cousins *UBVRI* filter as well as a Sloan *ugriz* filter; 1 hr exposure images have typical limiting magnitudes up to 24–25 mag (Djupvik & Andersen 2010).

NOT first obtained 2×120 s Sloan *r*-band frames of GRB 201223A starting at 02:21:52 UT on 2020 December 24th, i.e., 8.4 hr after the BAT trigger (Xu et al. 2020). Unfortunately, the optical afterglow is not detected in the stacked image, down to a limiting magnitude of $r \sim 22.0$. About 26.3 days after the BAT trigger, NOT obtained the images again at 00:57:31 UT on 2021 January 19th. Nine raw images were acquired and subsequently combined to enhance the signal-to-noise ratio. The exposure time for each image was 360 s. Through this process, no optical source was detected in our stacked image, down to a limiting magnitude of $r \sim 25.6$.

2.4. Optical Data Reductions

The raw images obtained from NEXT and NOT were processed by standard processes in the IRAF packages (Tody 1986), including bias and flat correction. The cosmic rays were also removed by the filtering described in Van Dokkum (2001). The measurements of magnitudes were conducted utilizing SourceExtractor (SExtractor, Bertin & Arnouts 1996), employing a circular aperture with a diameter of ten pixels. The magnitude was calibrated with Pan-STARRS1 (PS1, Chambers et al. 2016). All the photometric results are presented in Table 1.

For the Swift/UVOT data (Gropp et al. 2020), the afterglow was detected including white, *u*, *b* and *v* filters. We applied the standard HEAsoft software (version 6.31.1) and utilized the `uvotproduct` pipeline to reduce UVOT data with a source circular region of 5″ and a background region of 10″ aperture radius.

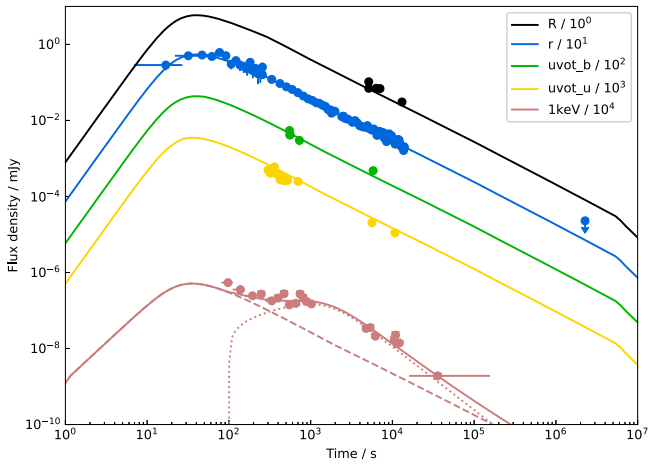

Figure 4. The best-fit light curve (solid lines) of GRB 201223A and multiband data (circular points) with error bar. The red dotted line corresponds to the contribution from BZ jet according to the fallback BH disk. The red dashed line corresponds to the external shock component in the X-ray band.

3. Multiband Analysis

3.1. Prompt Emission

The duration of GRB 201223A associated with the GBM trigger was $T_{90} = 33$ s (50–300 keV) and the event fluence (10–1000 keV) is $(2.1 \pm 0.3) \times 10^{-6}$ erg cm^{-2} from $T_0 - 17$ s to $T_0 + 13$ s (Wood & Team et al. 2020). We use three different models, namely Band, Blackbody, and Cutoff power-law, to fit the time-averaged spectrum. The best-fit parameters based on the Band model are $\alpha = -0.62^{+0.17}_{-0.16}$, $\beta = -2.93^{+0.38}_{-0.40}$, and $E_{\rm peak} = 137.36^{+23.59}_{-18.25}$ keV . The spectroscopic redshift was not reported and Xin et al. (2023) found that the redshift should be smaller than 1.85. If we use the redshift of $z = 1.85$ as an upper limit, then a high isotropic γ-ray energy $E_{\gamma,\rm iso} < 1.84 \times 10^{52}$ erg and isotropic γ-ray luminosity $L_{\gamma,\rm iso} < 2.34 \times 10^{51}$ erg s^{-1} are obtained.

We used the cross-correlation function (CCF) (Band 1997; Norris et al. 2000b; Ukwatta et al. 2010) and Monte Carlo simulation (Peterson et al. 1998; Ukwatta et al. 2010) to calculate the spectral lag and uncertainty of the burst (Norris et al. 2000a; Ukwatta et al. 2012). The result of the lag is 282 ± 264 ms between 15–85 and 85–160 keV with BAT data. For the Fermi data, the spectral lag is 225 ± 111 ms between 10–85 and 85–160 keV, which is consistent with the lag of BAT.

We also calculated the minimum variability timescale $t_{\rm mv} = 2.54$ s, which represents the rapid variation of prompt emissions in a short period of time (Vianello et al. 2018).

3.2. Afterglow Modeling

We compared the observed data with the theoretical framework. The *r*-band optical light curve is best described

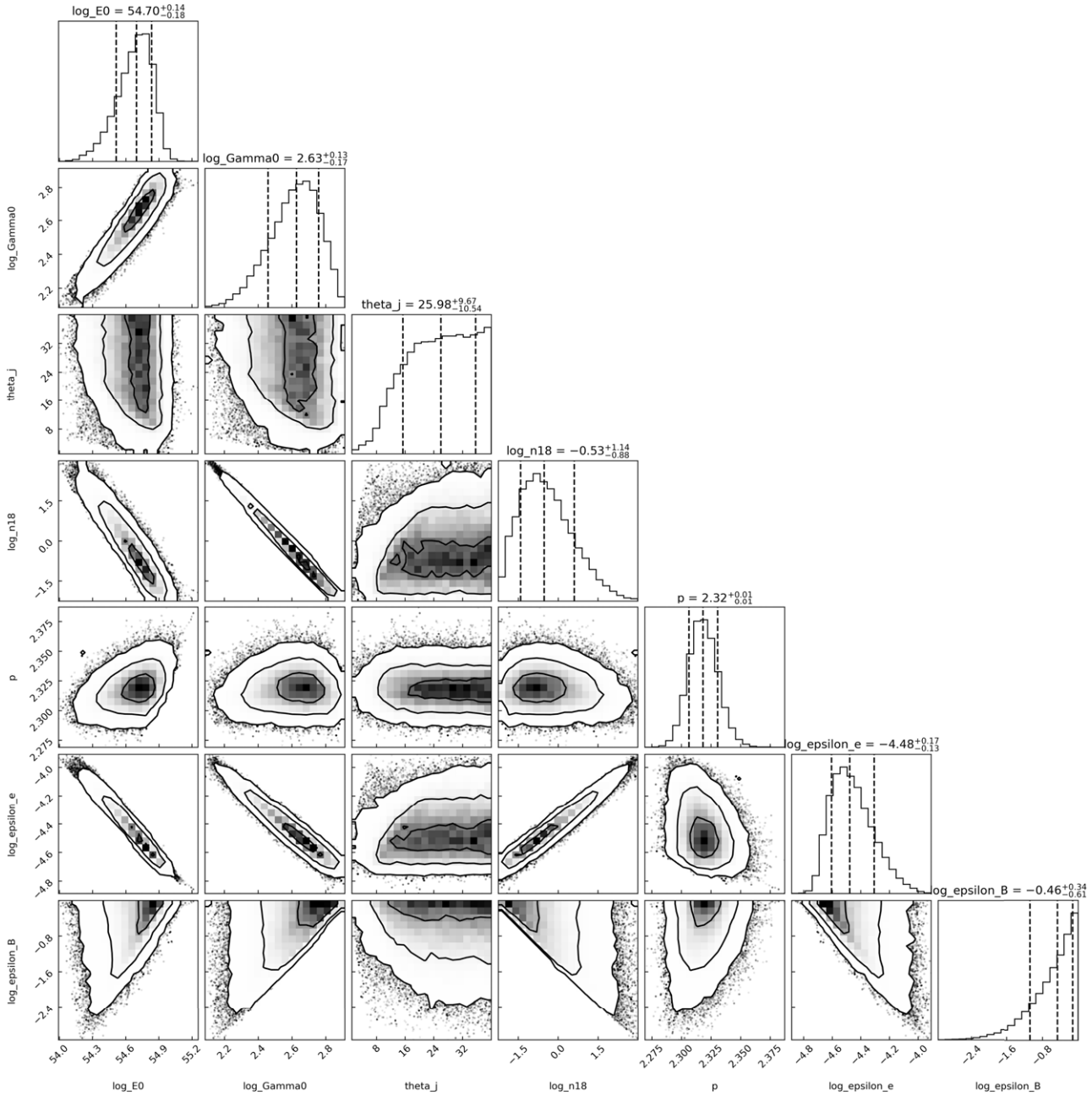

Figure 5. Posterior probability distributions of afterglow parameters.

by a broken power-law (BPL) with $\alpha_{r,1} = -0.88 \pm 1.04$, $\alpha_{r,2} = 1.09 \pm 0.01$ and break time at $t_{\rm b} = 54.1 \pm 28.5$ s. The spectral index is $\beta_{\rm opt} = 1.35 \pm 0.13$. The single power-law (SPL) is used to fit the X-ray light curve with an index of $\alpha_{\rm X} = 0.94 \pm 0.06$. The time-averaged spectrum gives the X-ray photon index $\Gamma = 1.91^{+0.35}_{-0.21}$, and the relation between the spectral index β and photon index Γ is $\beta = \Gamma - 1$. Therefore, the X-ray spectral index $\beta_{\rm X} = 0.91^{+0.35}_{-0.21}$ (Evans et al. 2009) which is consistent with the optical to X-ray spectral index $\beta_{\rm OX} = 0.96 \pm 0.03$.

We fit the multiband afterglow (optical and early X-ray) of GRB 201223A using `PyFRS`,[6] which can be used to calculate synchrotron light curves and spectra from external shocks (Gao et al. 2013; Wang et al. 2014; Lei et al. 2016; Zhu et al. 2023b;

[6] https://github.com/leiwh/PyFRS

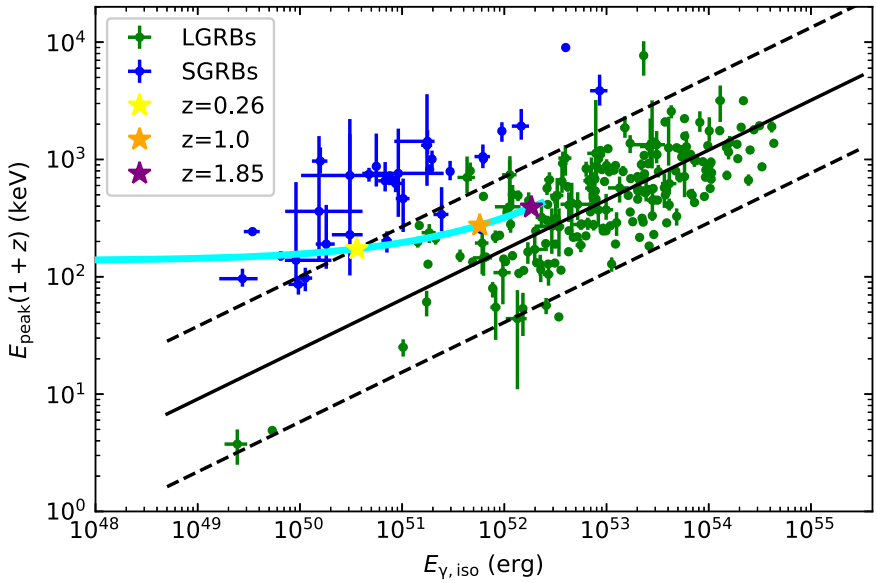

Figure 6. $E_{\rm p,i}$ vs. $E_{\gamma,\rm iso}$ diagram of GRBs. Blue points represent SGRBs and green points represent LGRBs. The solid black line is the best fit for LGRBs, while the dashed lines signify its 2σ distribution range. The cyan line shows the evolution of GRB 201223A with redshift. The three star symbols from left to right represent the positions at redshifts of 0.26 (yellow, lower limit), 1.0 (orange), and 1.85 (purple, upper limit) respectively.

Zhou et al. 2024). In this paper, the top-hat jet-type structure is used to model GRB 201223A. Since the burst redshift cannot be determined, we assume a typical GRB redshift of $z = 1.0$. We consider eight parameters including the isotropic kinetic energy $E_{\rm K,iso}$, the initial Lorentz factor Γ_0, the half-opening angle of the jet $\theta_{\rm j}$, the viewing angle $\theta_{\rm obs}$, the number density of the interstellar medium (ISM) n_0, the electron distribution power-law index p, the thermal energy fraction in magnetic field $\epsilon_{\rm B}$, and the thermal energy fraction in electrons $\epsilon_{\rm e}$. The observational angle was not effectively constrained due to the limitations of the available data, so we set $\theta_{\rm obs} = 0$ for simplicity.

We performed a parameter search with 30 walkers over 20,000 iterations, discarding the first 10,000 as burn-in steps. The prior types and ranges of each model parameter are listed in Table 2, and the optical afterglow light curves for GRB 201223A as well as the best-fit model are displayed in Figure 4. The corner plot of the model parameters is shown in Figure 5. The best fit of each parameter is given in Table 2 as: $E_{\rm K,iso} = 5.01^{+1.91}_{-1.70} \times 10^{54}$ erg, $\Gamma_0 = 426.58^{+148.86}_{-138.18}$, $\theta_{\rm j} = 25.98^{+9.67}_{-10.54}$ deg, $n_0 = 0.30^{+3.78}_{-0.26}$ cm^{-3}, $p = 2.32^{+0.01}_{-0.01}$, $\epsilon_{\rm e} = 3.31^{+1.59}_{-0.86} \times 10^{-5}$, $\epsilon_{\rm B} = 3.47^{+4.12}_{-2.62} \times 10^{-1}$.

4. Discussion

4.1. Redshift of the Burst

Due to the lack of spectroscopic observations for this burst, we cannot determine its exact redshift. However, since the target was detected in the Swift u-band, indicating the absence of Lyα absorption in this band, an upper limit of $z < 1.85$ can be placed on the redshift (Xin et al. 2023).

Amati et al. (2002) discovered a correlation between the isotropic-equivalent energy $E_{\gamma,\rm iso}$ and the intrinsic peak energy $E_{\rm p,i}$ of GRB prompt emission

$$E_{\rm p,i} = k(E_{\gamma,\rm iso}/10^{52}{\rm erg})^m, \quad (1)$$

where k and m are constants, and $E_{\rm p,i} = (1+z)E_{\rm p,obs}$. By plotting these two characteristic energies on a two-dimensional coordinate plane, two clusters of GRBs can be identified: short GRBs (SGRBs) with lower $E_{\gamma,\rm iso}$ but higher $E_{\rm p,i}$, and long GRBs (LGRBs) with higher $E_{\gamma,\rm iso}$ but lower $E_{\rm p,i}$. Since both characteristic energies require a precise redshift, conversely, we can estimate the redshift range of GRBs by the evolution of these two energies with redshift. We construct a $E_{\rm p,i} - E_{\gamma,\rm iso}$ sample containing 207 LGRBs and 33 SGRBs, as depicted in Figure 6.

GRB 201223A is identified as a typical LGRB based on its duration $T_{90} = 33$ s and the spectral lag 225 ms derived from Fermi data. Therefore, according to the 2σ range of LGRBs in Figure 6, we can obtain its redshift lower limit $z_{\rm low} \approx 0.26$. Of course, it cannot be ruled out that it is a peculiar GRB with special parameter values different from those of LGRBs. Thus, we propose a redshift range of 0.26–1.85 for GRB 201223A.

4.2. Central Engine Model

The X-ray light curve shows a shallow decay from 200 to 1000 s. The expected flux from the afterglow model is significantly lower than the observed value (see the red dashed

line in Figure 4). Two central engine models were considered to explain this light curve behavior: one is the spin-down of a magnetar, and the other is the fallback accretion onto a newborn BH. We will inspect these two central engine models by comparing with the afterglow data.

4.2.1. Spin-down of a Magnetar

The X-ray plateaus can be produced by the spin power of a millisecond magnetar (Dai & Lu 1998; Liang et al. 2007; Tang et al. 2019; Zhao et al. 2019). The characteristic spin-down luminosity L_0 can be written as

$$L_0 \simeq 1.0 \times 10^{49} \mathrm{erg\ s^{-1}} B_{\mathrm{p},15}^2 P_{0,-3}^{-4} R_6^6, \quad (2)$$

where $B_{\mathrm{p},15}$ is the magnetic field strength in units of 10^{15} G, $P_{0,-3}$ is the initial spin period in millisecond, and R_6 is the radius of the magnetar in units of 10^6 cm.

The evolution of the magnetar spin period due to dipole radiation is given by

$$P(t) = P_0\left(1 + \frac{t}{t_{\mathrm{md}}}\right)^{(1/2)}, \quad (3)$$

where the spin-down is dominated by the dipole radiation with timescale $t_{\mathrm{md}} \simeq 2.0 \times 10^3 s (I_{45} B_{\mathrm{p},15}^{-2} P_{0,-3}^2 R_6^{-6})$. We consider only the energy loss due to dipole radiation in this work. As the spin-down of magnetar, it may leave behind a stable NS, or collapses into a BH if it is temporarily supported by rigid rotation. The latter will lead to a sharp decay in X-ray flux as observed. The maximum gravitational mass of supermassive magnetars can be expressed as (Lasky et al. 2014)

$$M_{\mathrm{max}} = M_{\mathrm{TOV}}(1 + \hat{\alpha} P^{\hat{\beta}}), \quad (4)$$

where M_{TOV} is the maximum mass for a nonrotating NS. For the NS equation of state (EoS), in accordance with recent studies utilizing data from GRBs, we have chosen to utilize the EoS GM1, which specifies the radius of the magnetar $R = 12.05$ km, the rotational inertia $I = 3.33 \times 10^{45}$ g cm^{-2}, $\hat{\alpha} = 1.58 \times 10^{-10} s^{-\hat{\beta}}$ and $\hat{\beta} = -2.48$ (Lü et al. 2015; Gao et al. 2016b).

First, we assume that the re-brightening of the X-ray emission originates from energy injection into the forward shock, and find that the injection luminosity via X-ray afterglow fitting is 1.6×10^{53} erg s^{-1} at a redshift of $z = 1.0$. This value, however, severely exceeds the energy expected from a magnetar. Even adopting the lower redshift $z = 0.26$, the result does not change too much. Another point is that such energy injection will also lead to re-brightening in optical which is absent from observations.

We therefore consider that the re-brightening of the X-ray emission comes from internal dissipation of a magnetar, and derive the luminosity $L_{\mathrm{X}} \sim 3.35 \times 10^{45}$ erg s^{-1}, 5.37×10^{46} erg s^{-1} and 1.73×10^{47} erg s^{-1} for redshift of 0.26, 1.0 and 1.85, respectively.

Substituting these three X-ray luminosities as the spin-down luminosities of the magnetar into the above equation, i.e., $L_{\mathrm{X}} \sim L_0$, and assuming spin-down timescale $t_{\mathrm{md}} = 3000/(1+z)$ s, we obtain the spin periods of the magnetar to be 411 ms, 129 ms, and 86 ms for the redshift of 0.26, 1.0 and 1.85, respectively, and the surface magnetic fields of the magnetar to be 3.98×10^{17} G, 1.58×10^{17} G, and 1.25×10^{17} G for the redshift of 0.26, 1.0 and 1.85, respectively. Rowlinson et al. (2014) compiled a sample of GRB magnetars, with a maximum magnetar period of 83 ms and a surface magnetic field range of $\sim 3 \times 10^{14}$ to $\sim 2 \times 10^{17}$ G in the sample. While the results in the sample may vary due to different computational methods, we derived that the magnetic field and period of the magnetar associated with GRB 201223A are both outliers, lying at the edge of the sample. In our calculations, we assumed a relatively large spin-down timescale; if this value is decreased, the derived results would deviate even further from the sample. Therefore, the spin-down magnetar model for the re-brightening of X-ray emission is disfavored.

4.2.2. Fallback Accretion onto the Newborn BH

In the framework of BH central engine model, the X-ray plateau or bump seen in GRB 201223A is explained by the fallback accretion (Wu et al. 2013). An accretion system can generate relativistic jets through neutrino-antineutrino annihilation (Popham et al. 1999; Narayan et al. 2001; Janiuk et al. 2004; Gu et al. 2006; Chen & Beloborodov 2007; Lei et al. 2009; Xie et al. 2016) or the BZ mechanism (Blandford & Znajek 1977; Lee & Kim 2000; Li & Paczyński 2000; Lei et al. 2005b). We assume that the evolution of fallback accretion rate is described with a smooth BPL function (Chevalier 1989; MacFadyen et al. 2001; Zhang et al. 2008; Dai & Liu 2012),

$$\dot{M} = \dot{M}_{\mathrm{p}}\left[\frac{1}{2}\left(\frac{t - t_0}{t_{\mathrm{p}} - t_0}\right)^{-\frac{1}{2}} + \frac{1}{2}\left(\frac{t - t_0}{t_{\mathrm{p}} - t_0}\right)^{\frac{5}{3}}\right]^{-1}, \quad (5)$$

where t_0 is the beginning time of the fallback accretion in the local frame and t_{p} is the peak time of the fallback accretion. The early-time fallback accretion behavior follows $t^{1/2}$ and late-time fallback accretion behavior follows $t^{-5/3}$.

The BZ power can be rewritten as a function of mass accretion rate (Lei et al. 2013; Wu et al. 2013).

$$\dot{E}_{\mathrm{B}} = 9.3 \times 10^{53} \frac{a_\bullet^2 \dot{m} F(a_\bullet)}{(1 + \sqrt{1 - a_\bullet^2})^2} \mathrm{erg\ s^{-1}}, \quad (6)$$

$$F(a_\bullet) = [(1 + q^2)/q^2][(q + 1/q)\arctan q - 1]. \quad (7)$$

Here $q = a_\bullet/(1 + \sqrt{1 - a_\bullet^2})$, $a_\bullet = J_\bullet c/(GM_\bullet^2)$ is the BH spin parameter, and $\dot{m} = \dot{M}/(M_\odot\ \mathrm{s^{-1}})$ is the accretion rate.

Then we connect the observed X-ray luminosity to the BZ power through

$$\eta \dot{E}_{\mathrm{B}} = f_{\mathrm{b}} L_{\mathrm{X}}, \quad (8)$$

where η is the efficiency of converting BZ power to X-ray radiation and $f_{\rm b} = (1 - \cos\theta_{\rm j})/2$ is the beaming factor of the jet.

In the case of GRB 201223A, we assume a BH with a mass of $M_\bullet = 3M_\odot$, a spin of $a_\bullet = 0.9$, efficiency $\eta = 0.1$ and the calculation starts from $t_0 = 100/(1+z)$ s. We utilize the optimal parameters obtained from the afterglow fitting, which indicate a jet opening angle of 25° (Table 2), and thus $f_b \simeq 0.05$. The parameters for the fitting are $\dot{M}_{\rm p} \simeq 2.76 \times 10^{-9} M_\odot$ s^{-1}, $t_{\rm p} = 1637/(1+z)$ s, and the total fallback accreted mass $M_{\rm fb} \simeq 1.41 \times 10^{-6} M_\odot$ for the burst redshift of $z = 1.0$. Thus, we can estimate the minimum radius around which matter starts to fall back ($r_{\rm fb}$) from the following equation (Wu et al. 2013)

$$r_{\rm fb} \simeq 3.5 \times 10^{10} (M_\bullet/3M_\odot)^{1/3} (t_0/360\ {\rm s})^{2/3}\ {\rm cm}. \quad (9)$$

Then we estimate the value of $r_{\rm fb} \simeq 9.4 \times 10^9$ cm.

The best-fit X-ray light curve component due to fallback accretion is shown as a dotted line in Figure 4. The red solid line signifies the total emission by including the contributions from both the BZ jet (dotted line) and the external shock (dashed line). Across the redshift range of 0.26–1.85, the derived accretion rate and fallback radius fall within reasonable ranges. Consequently, the fallback accretion scenario provides a more plausible explanation for the X-ray light curve behavior of GRB 201223A.

5. Summary

We present our early optical observations of GRB 201223A with the NEXT and NOT facilities. The optical light curve exhibits a power-law decay, as predicted by the standard afterglow. However, the evolution of the X-ray light curve obtained by Swift/XRT shows a shallow decay from 200 to 1000 s, suggesting an additional radiation component beyond the afterglow. Our results are summarized as follows:

1. The time-resolved spectral analysis of the prompt emission of GRB 201223A reveals the best-fit parameters based on the Band model with $\alpha = -0.62^{+0.17}_{-0.16}$, $\beta = -2.93^{+0.38}_{-0.40}$, and $E_{\rm peak} = 137.36^{+23.59}_{-18.25}$ keV. We also calculate the spectral lag of this burst, which is 255 ± 111 ms. Combined with $T_{90} = 33$ s, we believe this is a typical LGRB originating from the collapse of a massive star.

2. The multiband afterglow fitting was performed using the Python package `PyFRS` with the best physical parameters: $E_{\rm K,iso} = 5.01^{+1.91}_{-1.70} \times 10^{54}$ erg, $\Gamma_0 = 426.58^{+148.86}_{-138.18}$, $\theta_{\rm j} = 25.98^{+9.67}_{-10.54}$ deg, $n_0 = 0.30^{+3.78}_{-0.26}$ cm^{-3}, $p = 2.32^{+0.01}_{-0.01}$, $\epsilon_{\rm e} = 3.31^{+1.59}_{-0.86} \times 10^{-5}$, $\epsilon_{\rm B} = 3.47^{+4.12}_{-2.62} \times 10^{-1}$.

3. The redshift of this burst is constrained to be less than 1.85 due to the detection of its afterglow in the u-band by Swift; and we further restrict its redshift to be greater than 0.26 by placing it within the LGRB region in the Amati diagrams.

4. We investigated two central engine models, spin-down magnetar and fallback accretion of BH, to account for the X-ray re-brightening phenomenon. Our findings indicate that the fallback accretion model provides a more natural explanation for this observation, with accretion rate of $\dot{M}_{\rm p} \simeq 2.76 \times 10^{-9} M_\odot$ s^{-1}, start time of $t_{0,i} = 50$ s and peak time of $t_{\rm p,i} = 819$ s at rest frame (assuming $z = 1.0$).

Acknowledgments

The data presented here were obtained in part with ALFOSC, which is provided by the Instituto de Astrofisica de Andalucia (IAA) under a joint agreement with the University of Copenhagen and NOT. This research has made use of the Spanish Virtual Observatory (http://svo.cab.inta-csic.es) supported by the MINECO/FEDER through grant AyA2017-84089.7. D.X. acknowledges the science research grants from the China Manned Space Project with NO. CMS-CSST-2021-A13 and CMS-CSST-2021-B11. W.H. Lei acknowledges support by the National Key R&D Program of China (No. 2020YFC2201400).

References

Abbott, B. P., Abbott, R., Abbott, T. D., et al. 2017, ApJL, 848, L12
Almeida, A., Anderson, S. F., Argudo-Fernández, M., et al. 2023, ApJS, 267, 44
Amati, L., Frontera, F., Tavani, M., et al. 2002, A&A, 390, 81
Band, D., Matteson, J., Ford, L., et al. 1993, ApJ, 413, 281
Band, D. L. 1997, ApJ, 486, 928
Barthelmy, S. D., Barbier, L. M., Cummings, J. R., et al. 2005, SSRv, 120, 143
Bertin, E., & Arnouts, S. 1996, A&AS, 117, 393
Blandford, R. D., & Znajek, R. L. 1977, MNRAS, 179, 433
Chambers, K. C., Magnier, E., Metcalfe, N., et al. 2016, arXiv:1612.05560
Chen, W., Xie, W., Lei, W.-H., et al. 2017, ApJ, 849, 119
Chen, W.-X., & Beloborodov, A. M. 2007, ApJ, 657, 383
Chevalier, R. A. 1989, ApJ, 346, 847
Costa, E. e., Frontera, F., Heise, J., et al. 1997, Natur, 387, 783
Dai, Z., & Lu, T. 1998, arXiv:astro-ph/9810402
Dai, Z. G., & Liu, R.-Y. 2012, ApJ, 759, 58
Dey, A., Schlegel, D. J., Lang, D., et al. 2019, AJ, 157, 168
Djupvik, A. A., & Andersen, J. 2010, Highlights of Spanish Astrophysics V (Berlin: Springer), 211
Evans, P., Beardmore, A., Page, K., et al. 2009, MNRAS, 397, 1177
Galama, T. J., Vreeswijk, P. M., van Paradijs, J., et al. 1999, A&AS, 138, 465
Gao, H., Lei, W.-H., You, Z.-Q., & Xie, W. 2016a, ApJ, 826, 141
Gao, H., Lei, W.-H., Zou, Y.-C., Wu, X.-F., & Zhang, B. 2013, NewAR, 57, 141
Gao, H., Zhang, B., & Lü, H.-J. 2016b, PhRvD, 93, 044065
Gehrels, N., Chincarini, G., Giommi, P., et al. 2004, ApJ, 611, 1005
Gropp, J. D., Barthelmy, S. D., Kennea, J. A., et al. 2020, GCN, 29158, 1
Gu, W.-M., Liu, T., & Lu, J.-F. 2006, ApJ, 643, L87
Janiuk, A., Perna, R., Di Matteo, T., & Czerny, B. 2004, MNRAS, 355, 950
Kouveliotou, C., Meegan, C. A., Fishman, G. J., et al. 1993, ApJ, 413, L101
Lasky, P. D., Haskell, B., Ravi, V., Howell, E. J., & Coward, D. M. 2014, PhRvD, 89, 047302
Lee, H. K., & Kim, H.-K. 2000, arXiv:astro-ph/0008360
Lei, W., Wang, D., Zhang, L., et al. 2009, ApJ, 700, 1970
Lei, W.-H., Wang, D.-X., & Ma, R.-Y. 2005a, ApJ, 619, 420
Lei, W.-H., Wang, D.-X., & Ma, R.-Y. 2005b, ChJAA, 5, 279
Lei, W.-H., Yuan, Q., Zhang, B., & Wang, D. 2016, ApJ, 816, 20
Lei, W.-H., Zhang, B., & Liang, E.-W. 2013, ApJ, 765, 125
Li, L.-X., & Paczyński, B. 2000, ApJ, 534, L197

Liang, E.-W., Zhang, B.-B., & Zhang, B. 2007, ApJ, 670, 565
Liu, T., Gu, W.-M., & Zhang, B. 2017, NewAR, 79, 1
Liu, T., Hou, S.-J., Xue, L., & Gu, W.-M. 2015, ApJS, 218, 12
Lü, H.-J., Zhang, B., Lei, W.-H., Li, Y., & Lasky, P. D. 2015, ApJ, 805, 89
MacFadyen, A. I., Woosley, S. E., & Heger, A. 2001, ApJ, 550, 410
Meegan, C., Lichti, G., Bhat, P. N., et al. 2009, ApJ, 702, 791
Narayan, R., Piran, T., & Kumar, P. 2001, ApJ, 557, 949
Norris, J., Marani, G., & Bonnell, J. 2000a, ApJ, 534, 248
Norris, J. P., Marani, G. F., & Bonnell, J. T. 2000b, ApJ, 534, 248
Paciesas, W. S., Meegan, C. A., Pendleton, G. N., et al. 1999, ApJS, 122, 465
Peterson, B. M., Wanders, I., Horne, K., et al. 1998, PASP, 110, 660
Planck Collaboration, Ade, P. A. R., Aghanim, N., et al. 2014, A&A, 571, A16
Popham, R., Woosley, S. E., & Fryer, C. 1999, ApJ, 518, 356
Roming, P. W. A., Kennedy, T. E., Mason, K. O., et al. 2005, SSRv, 120, 95
Rowlinson, A., Gompertz, B. P., Dainotti, M., et al. 2014, MNRAS, 443, 1779
Tang, C.-H., Huang, Y.-F., Geng, J.-J., & Zhang, Z.-B. 2019, ApJS, 245, 1
Tody, D. 1986, Proc. SPIE, 0627, 733
Ukwatta, T., Dhuga, K. S., Stamatikos, M., et al. 2012, MNRAS, 419, 614
Ukwatta, T. N., Stamatikos, M., Dhuga, K. S., et al. 2010, ApJ, 711, 1073
Van Dokkum, P. G. 2001, PASP, 113, 1420
Vestrand, W. T., Wren, J., Wozniak, P., et al. 2006, Natur, 442, 172
Vianello, G., Gill, R., Granot, J., et al. 2018, ApJ, 864, 163
Vianello, G., Lauer, R. J., Younk, P., et al. 2015, arXiv:1507.08343
Wang, J.-Z., Lei, W.-H., Wang, D.-X., et al. 2014, ApJ, 788, 32
Wood, J. & Fermi GBM Team 2020, GCN, 29161, 1
Woosley, S. E., & Bloom, J. S. 2006, ARA&A, 44, 507
Wright, E. L., Eisenhardt, P. R. M., Mainzer, A. K., et al. 2010, AJ, 140 1868
Wu, X.-F., Hou, S.-J., & Lei, W.-H. 2013, ApJL, 767, L36
Xie, W., Lei, W.-H., & Wang, D.-X. 2016, ApJ, 833, 129
Xin, L., Han, X., Li, H., et al. 2023, NatAs, 7, 724
Xu, D., Malesani, D., Galindo, P., et al. 2020, GCN, 29169, 1
Zhang, B. 2018, The Physics of Gamma-ray Bursts (Cambridge: Cambridge Univ. Press)
Zhang, B., Zhang, B.-B., Virgili, F. J., et al. 2009, ApJ, 703, 1696
Zhang, W., Woosley, S. E., & Heger, A. 2008, ApJ, 679, 639
Zhao, L., Gao, H., Lei, W., Lan, L., & Liu, L. 2021, ApJ, 906, 60
Zhao, L., Liu, L., Gao, H., et al. 2020, ApJ, 896, 42
Zhao, L., Zhang, B., Gao, H., et al. 2019, ApJ, 883, 97
Zhao, L.-T. 2023, RAA, 23, 115014
Zhou, C., Zhu, Z.-P., Lei, W.-H., et al. 2024, ApJ, 963, 66
Zhu, Z., Fu, S., Zhang, M., et al. 2020, GCN, 29159, 1
Zhu, Z.-P., Xu, D., Fynbo, J. P., et al. 2023a, ApJ, 948, 30
Zhu, Z.-P., Xu, D., Fynbo, J. P. U., et al. 2023b, ApJ, 948, 30